High-frequency surface and body waves from ambient noise cross-correlations at Long Beach, CA

Jason P. Chang, Sjoerd de Ridder, and Biondo Biondi

ABSTRACT

The density and duration of the Long Beach, California passive seismic array makes it well-suited for exploiting ambient noise to estimate inter-station Green's functions at frequencies (3–9 Hz) that are well beyond the microseism band. Using the ambient noise cross-correlation technique, we are able to recover and identify Rayleigh-wave and body-wave energy at these frequencies. From virtual-source gathers along a line of receivers running north-south, we find that Rayleigh-wave energy is primarily generated by traffic noise on busy streets and Interstate 405. Group-velocity dispersion images and analysis of group arrival time as a function of virtual source-receiver azimuth suggest that this Rayleigh-wave energy has the potential to be used as input to a 2D transmission tomography workflow. By summing over different virtual source-receiver azimuths, we determine the direction the body-wave energy is arriving from. By looking at correlation results from various patches of virtual source-receiver pairs, we find that body-wave energy is strongest in certain parts of the array.

INTRODUCTION

Over the past decade, ambient noise cross-correlation has proven to be an effective method for estimating the Green's function between two receivers at the regional and continental scales (Yang et al., 2008; Bensen et al., 2008). While surface-wave energy typically dominates the recovered response, body waves have been retrieved in some cases (Roux et al., 2005; Zhan et al., 2010; Poli et al., 2012). With seismic arrays becoming larger and denser, there is an unprecedented opportunity to recover signal at frequencies higher than 2 Hz, which is beyond the microseism band. At these high frequencies, we can begin to separate surface waves and body waves. Surface waves at these frequencies can be important for fields such as engineering seismology, while body waves are necessary for any type of subsurface reflection imaging.

In January 2012, NodalSeismic deployed a dense seismic array in Long Beach, California (Figure 1). The array spans a 8.5×4 km region and consists of 2400 vertical-component geophones spaced an average of 100 m apart. The geophones were continuously recording (24 hrs/day) for over three months. Because the array is located along the coast and in an urban environment, it is dominated by coastal

energy at low frequencies (below 2 Hz) and by anthropogenic sources within the array at high frequencies (above 2 Hz). Studies have already demonstrated success at extracting surface waves below 4 Hz from Phase 1 (Lin et al., 2012, 2013) and Phase 2 (Chang et al., 2013). In Phase 1, Lin et al. (2012, 2013) also observed body waves when stacking over multiple virtual sources.

In this study, we focus on recovering correlated energy between 3 and 9 Hz, which is beyond the frequency range that has previously been investigated at this site. We begin with a brief overview of our ambient noise cross-correlation method. We then show that high-frequency Rayleigh waves dominate the estimated Green's functions (EGFs) between individual virtual source-receiver pairs. To verify where this energy comes from, we look at virtual-source gathers along a seismic line. We then examine whether these recovered Rayleigh waves are reliable enough for use in a transmission tomography workflow by generating group-velocity dispersion images and calculating group arrival times as a function of virtual source-receiver azimuth. We also show that we can recover body waves when stacking over multiple virtual-source gathers. To determine the direction they are coming from, we stack correlations over different virtual source-receiver azimuths. To determine where the energy of these body waves is strongest, we stack correlations contained in patches throughout the array.

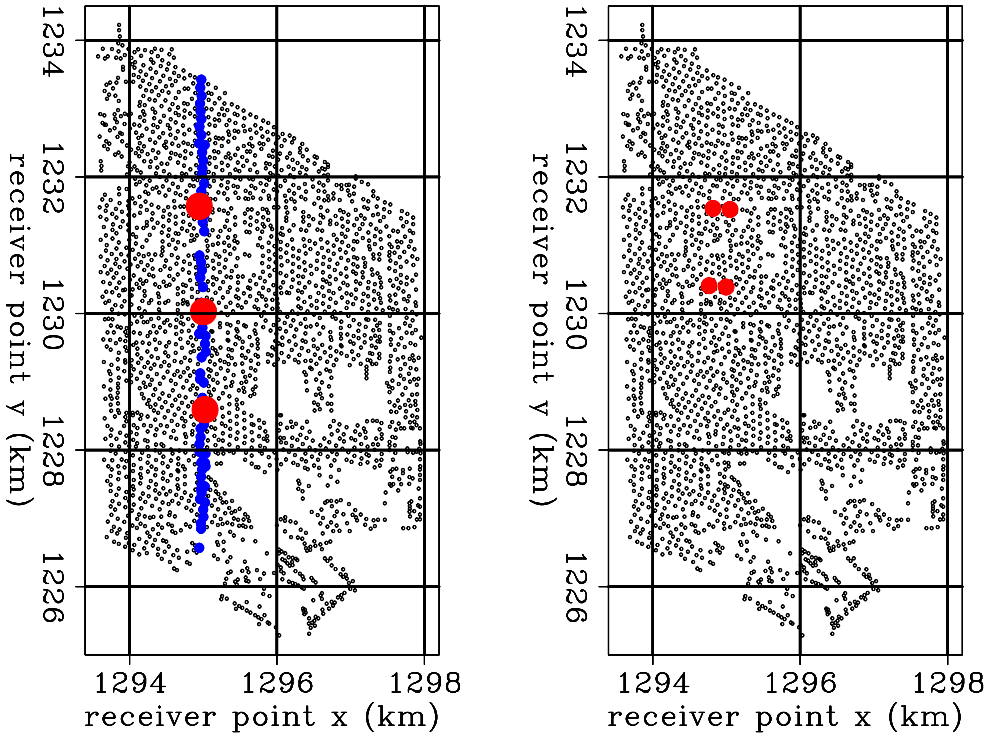

Figure 1: Maps of the Long Beach array. Left: Blue line indicates receivers used for creating virtual-source gathers at the locations indicated by the red dots. Right: Virtual source locations used for creating group-velocity dispersion images, indicated by red dots. Coordinates are NAD27, CA State Plane, Zone 7, kilometers. [**ER**]

AMBIENT NOISE CROSS-CORRELATION

Cross-correlating continuous and simultaneous recordings of ambient seismic noise from two receivers produces the full estimate of the Green's function and its time-

reversed version between those two receivers, convolved with the autocorrelation of a source function (Wapenaar et al., 2010; Wapenaar and Fokkema, 2006). Here, we implement a processing method adapted from Bensen et al. (2007). We first break up our time series into tapered, non-overlapping two-hour time windows and then whiten the input traces prior to cross-correlating. In the frequency domain, the cross-correlation of pre-whitened traces can be expressed as:

$$[G(x_B, x_A, \omega) + G^*(x_B, x_A, \omega)] = \left\langle \left(\frac{U(x_B, \omega)}{\{|U(x_B, \omega)|\}} \right) \left(\frac{U^*(x_A, \omega)}{\{|U(x_A, \omega)|\}} \right) \right\rangle, \quad (1)$$

where G is the Green's function between two receiver locations (x_A, x_B), $U(x, \omega)$ is the spectrum of the wavefield at a given receiver location x, $*$ represents the complex conjugate, $\langle \cdot \rangle$ represents the time-averaged ensemble, $|\cdot|$ represents the real absolute value of the spectrum, and $\{\cdot\}$ represents a 0.003 Hz running window average used for whitening the signal. We then normalize the resulting correlation from each two-hour time window before stacking to dampen the effect of spurious events. Finally, we bandpass the correlation for the frequency range of interest. This method is effective where trace-to-trace amplitudes are highly variable because it balances the amplitude information while maintaining the phase information of the correlations.

HIGH-FREQUENCY SURFACE WAVES

Using the cross-correlation technique on ambient noise at Long Beach, Chang et al. (2013) showed it was possible to recover Rayleigh waves between 2 and 4 Hz. From power spectral density maps, it appeared that anthropogenic sources dominated the noise field at these frequencies. From beamforming, it appeared that traffic energy, particularly from Interstate 405, was the dominant noise source in the region. Here, we create virtual-source gathers along a line of receivers to observe the effect of these noise sources on the ambient noise cross-correlation results. We then examine group-velocity dispersion images and group arrival times as a function of virtual source-receiver azimuth to determine the suitability of these high-frequency Rayleigh waves for use in a transmission tomography workflow.

Virtual-source gathers

We apply ambient noise cross-correlation to recordings from receivers along a north-south line that is perpendicular to Interstate 405. We choose three receivers (red dots in Figure 1a) to be our virtual sources: one centered at Interstate 405 (northern-most receiver), one in the middle of the array, and one centered at E 7th St (southern-most receiver). Virtual-source gathers for these locations are shown in Figures 2a, 2b, and 2c, respectively. Each gather is created from 35-days worth of correlations and contains frequencies between 3 and 5 Hz. We sort the traces into 100 m offset bins.

In each of these figures, we see fundamental-mode Rayleigh waves dominating the EGFs and traveling at approximately 250 m/s. We also see the first-order Rayleigh-wave mode traveling at approximately 400 m/s when the virtual source is located at E 7th St (Figure 2c). Two observations indicate that the correlated energy we are recovering at these frequencies is generated by traffic noise. One is that virtual-source gathers centered on roads/highways (Figures 2a and 2c) show very little correlated energy at acausal time lags. This indicates that energy is primarily propagating away from those virtual sources, or, in other words, traffic energy is propagating away from roads and highways. Another observation is the presence of sharp peaks in the source gather between E 7th St and the highway (Figure 2b). These peaks are indicative of nearby active sources, and their offsets from the source location (2 km north and 1.5 km south) correspond to Interstate 405 and E 7th St, respectively.

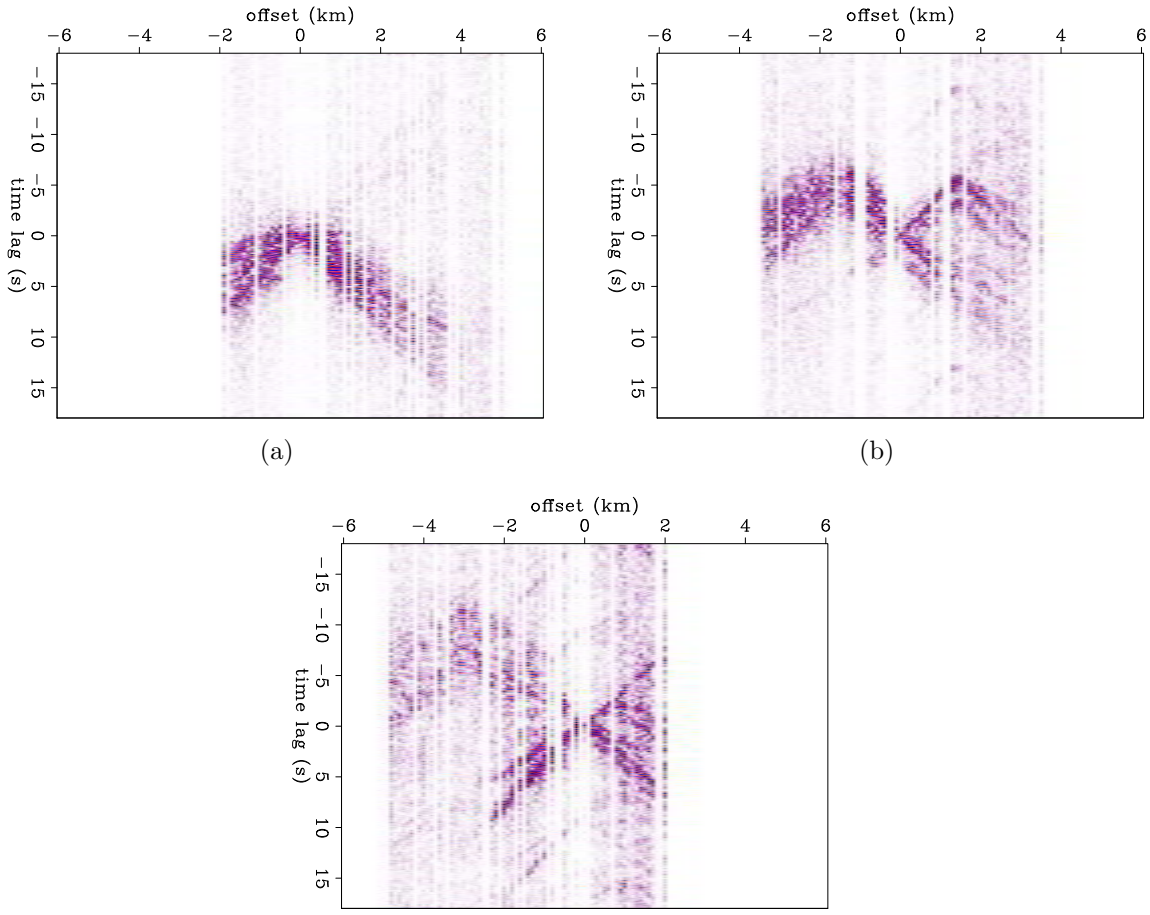

Figure 2: Virtual-source gathers for frequencies between 3 and 5 Hz from the three receiver locations depicted by red dots in Figure 1a. a) Northern-most station (centered at the highway), b) middle station, and c) southern-most station (centered at E 7th St). Negative offsets are toward the north, while positive offsets are toward the south. [**CR**]

Thus, our ambient noise cross-correlations reveal that EGFs at frequencies be-

tween 3 and 5 Hz are dominated by Rayleigh waves. While beamforming results from (Chang et al., 2013) suggests that most of the noise energy is generated by Interstate 405, EGFs along a line of receivers perpendicular to the highway suggests that other roads, such as E 7th St, also generate strong signal that can be used for subsurface imaging. However, this road could appear strong because it runs through a golf course, which is a relatively quiet region that would allow traffic energy to be picked up clearly. Although we prefer noise sources to be far away from and spatially well-distributed around the receivers when performing ambient noise cross-correlation, we can still extract reliable Green's functions as long as the noise sources are in the Fresnel zones.

Group velocity dispersion and travel time analysis

To examine the reliability of the estimated Rayleigh waves from traffic noise, we produce group-velocity dispersion images in the slowness-frequency domain and measure arrival times as a function of virtual source-receiver azimuth. To create these dispersion images, we begin by taking the analytic signal of one of our EGFs and applying a series of narrow bandpass Gaussian filters. In the frequency domain, the bandpassed analytic signal $S_a(\omega, \omega_0)$ is given as:

$$S_a(\omega, \omega_0) = S(\omega)(1 + \mathrm{sgn}(\omega))G(\omega - \omega_0), \tag{2}$$

where ω is frequency, ω_0 is the central frequency, $S(\omega)$ is the frequency-domain representation of the EGF, and $G(\omega - \omega_0)$ is a Gaussian filter given by:

$$G(\omega - \omega_0) = e^{-\alpha\left(\frac{\omega-\omega_0}{\omega_0}\right)^2}. \tag{3}$$

α is a modifiable parameter that determines resolution in the frequency and time domains. For the inter-station distances shown here (1.1 km), we choose α to be 50. We then inverse Fourier transform the signal $S_a(\omega, \omega_0)$ to the time domain, average the positive and corresponding negative time lags, and take the complex absolute value to obtain the smooth envelope of the EGF. Examples of envelopes for normalized 3.65 Hz EGFs are shown in Figure 3. Whereas a correlation parallel to the highway reveals only the fundamental-mode arrival at 5 s (Figure 3a), a correlation perpendicular to the highway shows both the fundamental-mode arrival at 5 s and the first-order mode arrival at 3 s (Figure 3b).

For a given EGF, envelopes can be plotted for many frequencies to produce a time-frequency plot, which can then be transformed into a group-velocity dispersion image (in the slowness-frequency domain) by dividing the time axis by the distance between the virtual source and receiver. Figure 4 shows dispersion images for the two northern virtual sources near the highway (Figure 1b). The left column corresponds to the western virtual source and the right column to the eastern virtual source. The top row corresponds to the receiver due south of the respective virtual source and the right column to the receiver due east. Similarly, Figure 5 shows dispersion images

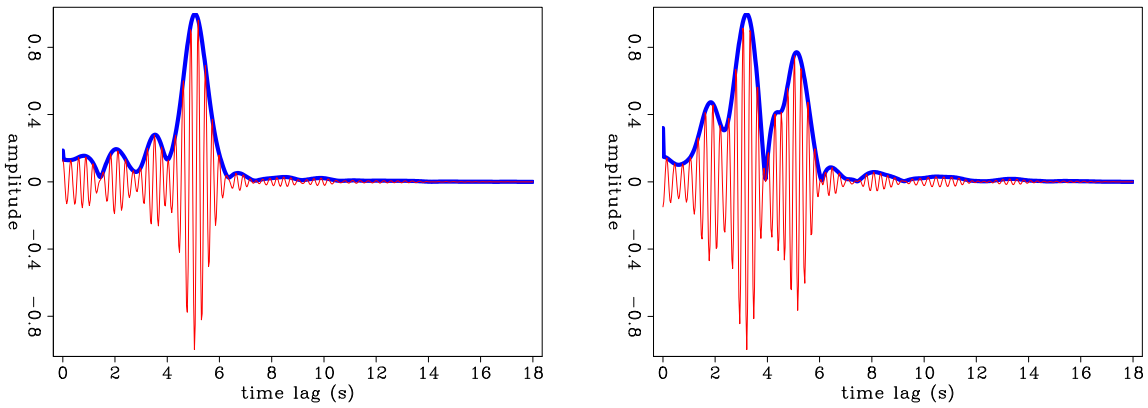

Figure 3: Estimated Green's functions and corresponding envelopes between a virtual source near Interstate 405 and a receiver a) 1.1 km due east, and b) 1.1 km due south. [**CR**]

for the two southern virtual sources away from the highway (Figure 1b). Rows and columns represent nearly the same virtual source-receiver orientations, with the sole difference being that the top row corresponds to receivers due north (instead of due south) of the respective virtual source.

There are a few observations to make from these dispersion images. First, the dispersion images generally show slowness increasing (velocity decreasing) as frequency increases. This is the result we expect and indicates that these estimated Rayleigh waves are potentially reliable. Second, nearly all dispersion images show distinguishable peaks up to at least 5 Hz, which suggests that we are able to resolve Rayleigh-wave arrivals at frequencies well beyond the microseism band. The exceptions to this pattern are EGFs between virtual source-receiver pairs away from the highway and spanning east-west (Figures 5c and 5d). This is because the highway is the dominant source of energy at these high frequencies (Chang et al., 2013). Thus, if both the virtual source and the receiver are far away from this energy source, we should not expect to find correlated energy at high frequencies. The third observation is that EGFs from nearby and parallel virtual source-receiver orientations produce similar dispersion images. This suggests that we are recovering consistent and stable EGFs that are truly sensitive to the subsurface they travel through. The fourth observation is that the dispersion image for EGFs from virtual source-receiver pair orientations parallel to the highway are smoother than EGFs from orientations perpendicular to the highway. A possible reason for this is that there is more highway energy in the Fresnel zones when the virtual source-receiver orientation is parallel to the highway (as long as the highway extends past the virtual source-receiver pair). This observation suggests that we can use EGFs from multiple virtual source-receiver orientations in a transmission tomography workflow.

To further examine the reliability of EGFs, we plot estimated group arrival times

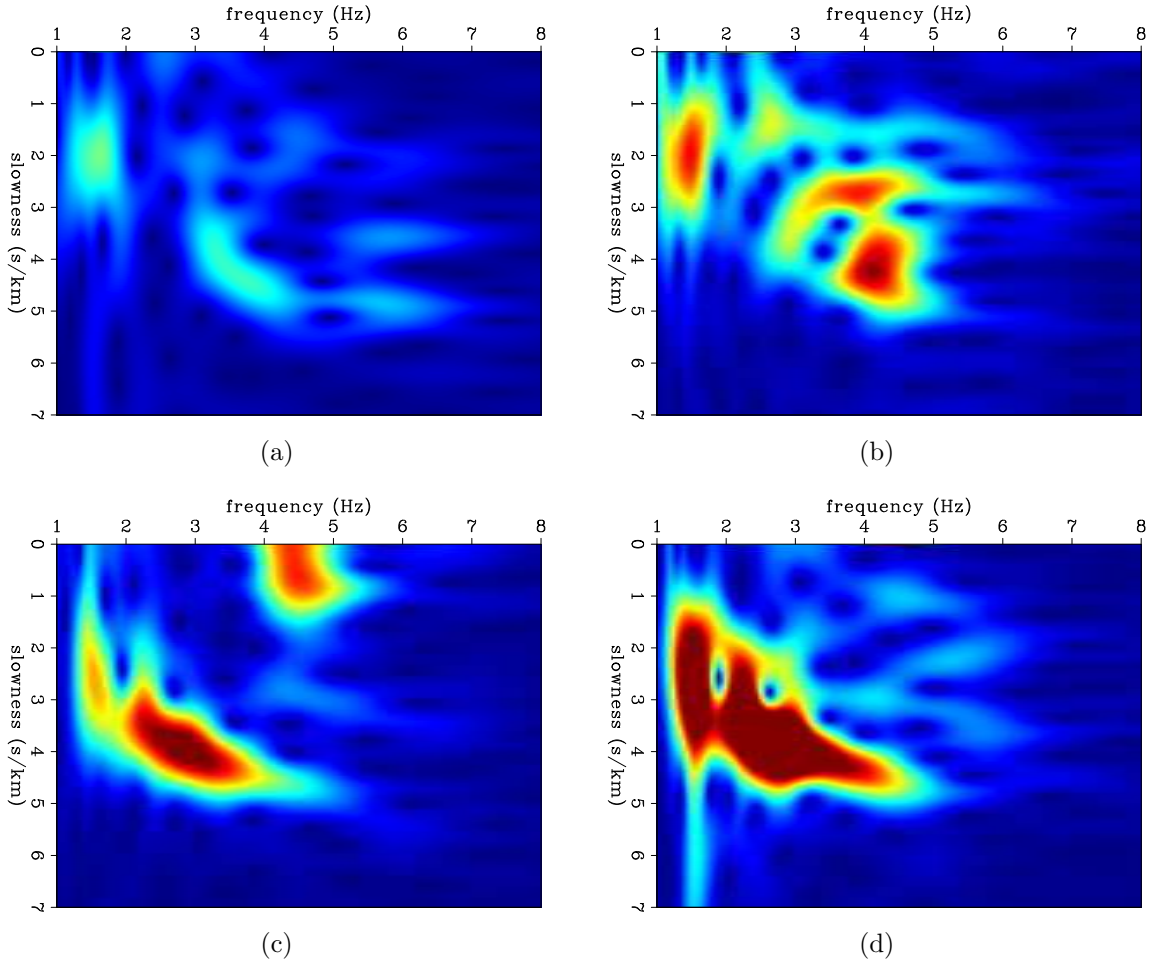

Figure 4: Group-velocity dispersion images in the slowness-frequency domain derived from EGFs. Left column: western virtual source near the highway. Right column: eastern virtual source near the highway. Top row: receiver due south of the respective virtual source. Bottom row: receiver due east of the respective virtual source. [**CR**]

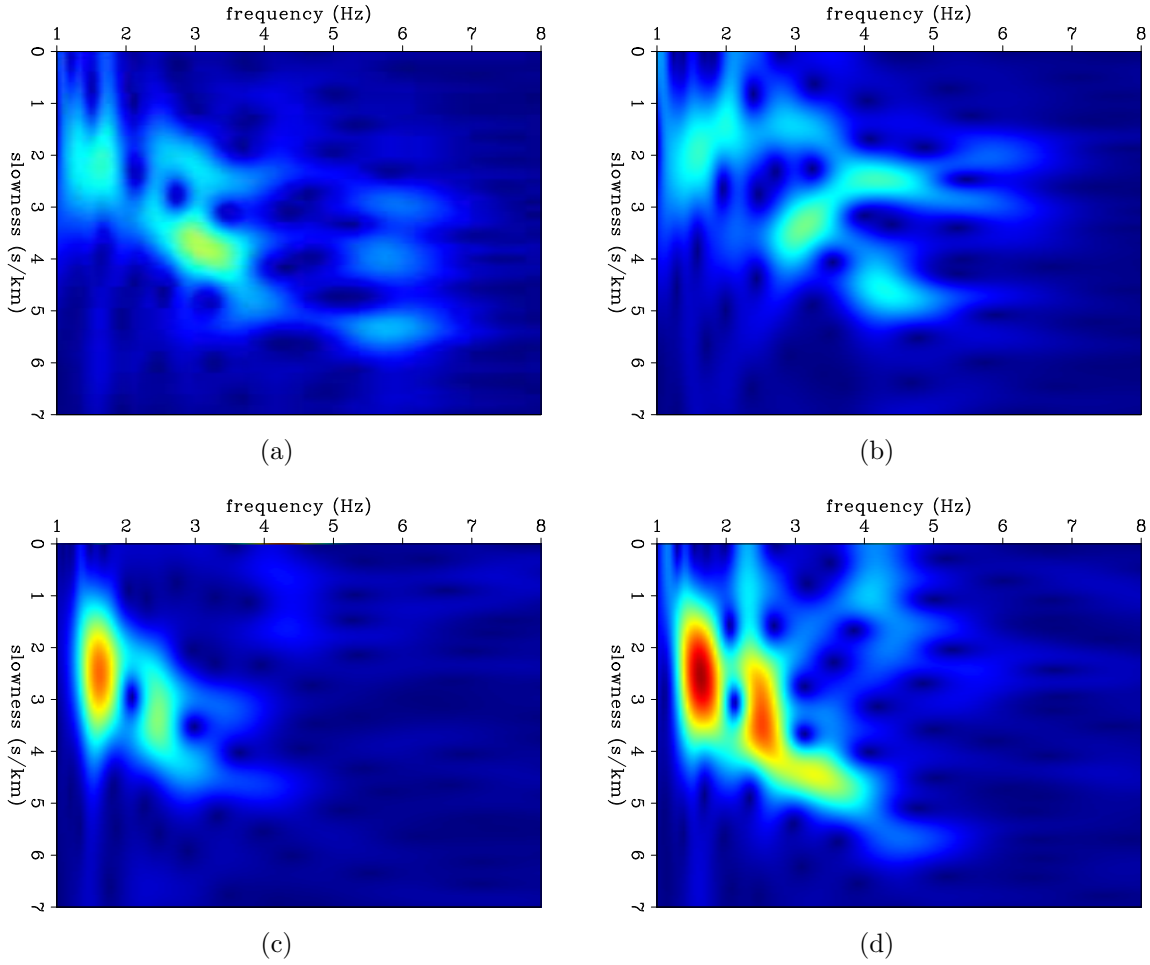

Figure 5: Group-velocity dispersion images in the slowness-frequency domain derived from EGFs. Left column: western virtual source away from the highway. Right column: eastern virtual source away from the highway. Top row: receiver due north of the respective virtual source. Bottom row: receiver due east of the respective virtual source. [**CR**]

at 4 Hz as a function of virtual source-receiver azimuth. Group arrival time is chosen to be when the envelope of the EGF is at its maximum. Figure 6a shows arrival times between the western virtual source near the highway and receivers 1.1 km toward the south (virtual source-receiver azimuths between -180 and 0 degrees); Figure 6b is similar but for the eastern virtual source near the highway. We see that arrival times are typically between 4 and 5 s along all shown azimuths (most of the outliers can be attributed to the first-order mode). The consistency between the two plots reinforces the previous claim that our EGFs near the highway are stable and reliable. The consistency within each plot reinforces the suggestion that we will be able to use EGFs along multiple azimuths as input into a transmission tomography workflow.

Figure 6c shows arrival times between the western virtual source away from the highway and receivers 1.1 km toward the north (virtual source-receiver azimuths between 0 and 180 degrees); Figure 6d is similar but for the eastern virtual source away from the highway. We see that arrival times vary significantly over azimuth. Arrival times around 90 degrees (receivers toward the north) are more reasonable than arrival times around 0 and 180 degrees (receivers toward the east and west, respectively), which reinforces the previous observation that EGFs at these frequencies become more reliable as either the virtual source or the receiver moves closer toward the highway. Therefore, based on group-velocity dispersion images and plots of estimated group arrival times as a function of source-receiver azimuth, we believe that recovered Rayleigh waves up to 5 Hz are generally reliable enough to be used as input into a transmission tomography workflow. This is particularly true when either the virtual source or the receiver is close to the highway.

BODY WAVES

Ambient noise cross-correlation theory states that the full Green's function between two receivers can be recovered under ideal conditions (Wapenaar and Fokkema, 2006). However, the resulting EGFs are typically dominated by surface-wave energy because noise sources are often located on the surface and because surface-wave amplitudes decay less rapidly than body-wave amplitudes. To boost the body-wave energy in our correlations, we stack over all virtual-source gathers. Correlations are sorted into 50 m offset bins, bandpassed for frequencies between 4 and 9 Hz, and averaged over causal and acausal time lags. The resulting gather, which we call a virtual super-source gather, is shown in Figure 7.

From the virtual super-source gather created from 35 days of data, we see body waves traveling between 2 km/s and 2.75 km/s. The curvature of the faster body wave is characteristic of diving waves, while the slower body wave is more linear and could thus be a refraction event. However, because we are stacking over all virtual sources, there is no spatial resolution. Instead, we attempt to address the following two questions: 1) What directions are the body waves coming from? 2) Where are the body waves strongest in the array?

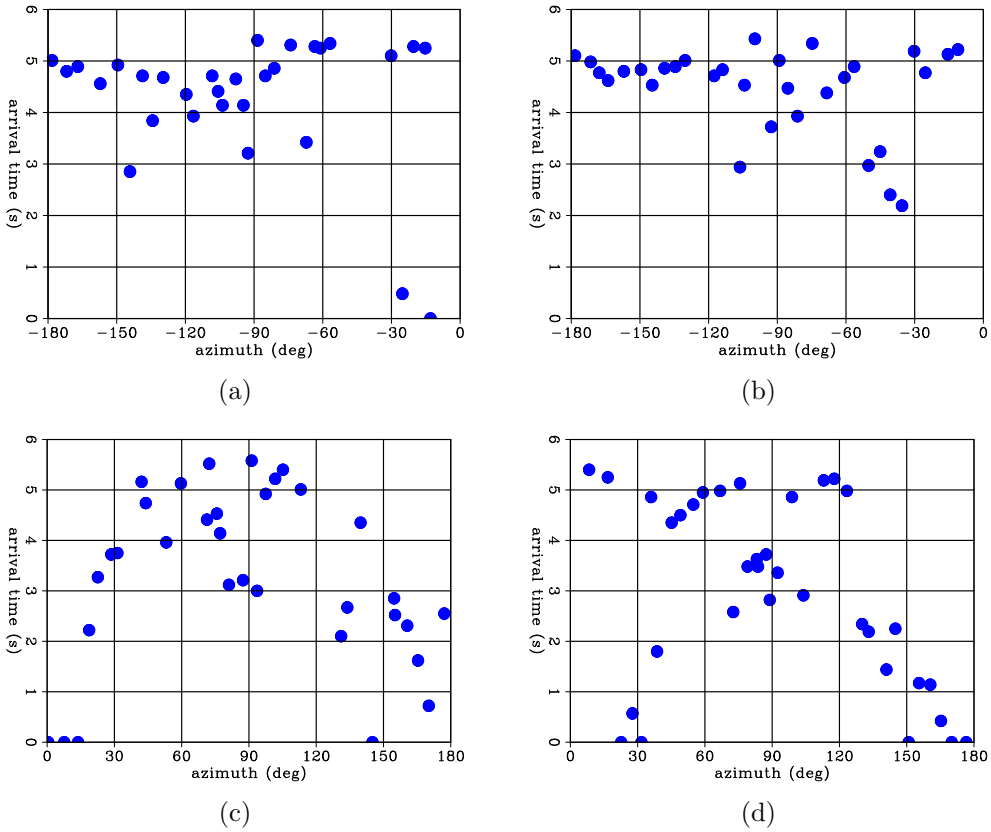

Figure 6: Plot of estimated arrival time vs. virtual source-receiver azimuth. 90 degrees corresponds to due north, 0 degrees corresponds to due east, and −90 degrees corresponds to due south. a) Western virtual source near highway. b) Eastern virtual source near highway. c) Western virtual source away from highway. d) Eastern virtual source away from highway. [**CR**]

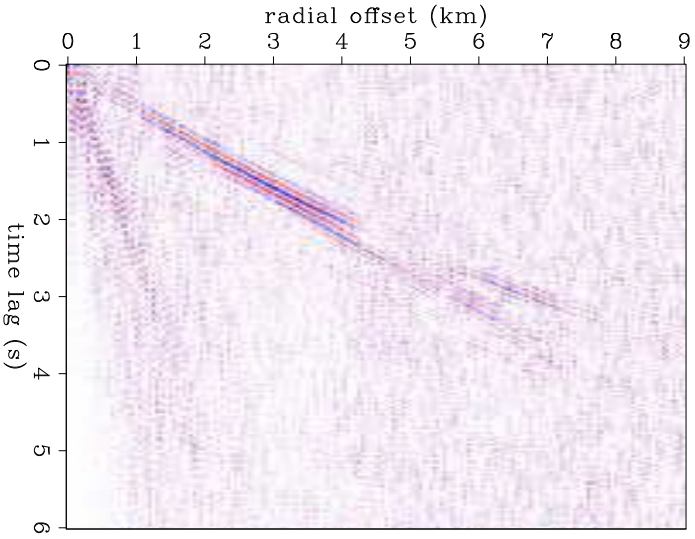

Figure 7: Virtual super-source gather created from stacking over all virtual-source gathers. The frequency range is 4–9 Hz. Body waves are clearly seen. [**CR**]

Directionality

Body-wave energy is not strong enough to be picked up by beamforming of the raw ambient noise. Therefore, to determine what direction the body waves are coming from, we sort our correlations by virtual source-receiver pair azimuth and stack them into 10-degree bins. Azimuth is defined as the angle of the receiver with respect to the virtual source, with -90 degrees corresponding to a receiver due south of the source and 90 degrees corresponding to a receiver due north of the source. We also keep causal and acausal time lags, rather than average them, to help the interpretation of our resulting partial super-source gathers.

Figure 8 shows four resulting partial super-source gathers for different azimuths and different frequency ranges. The top row (Figures 8a and 8b) corresponds to gathers for frequencies between 4.0 and 9.0 Hz, while the bottom row (Figures 8c and 8d) corresponds to gathers for frequencies between 0.5 and 2.0 Hz. Lower-frequency gathers are shown to aid interpretation of the higher-frequency gathers. The left column (Figures 8a and 8c) corresponds to azimuths between -55 and -65 degrees (receivers south-southeast of the virtual source), while the right column (Figures 8b and 8d) corresponds to azimuths between and -95 and -85 degrees (receivers south of the virtual source). These trends are apparent in each day of correlations.

The first observation is that none of these gathers are symmetric over zero time lag. Because events at acausal time lags correspond to energy moving toward the virtual source while events at causal time lags correspond to energy moving away from the virtual source, it is clear that noise sources are unevenly distributed in space for these two frequency bands. Looking at the lower frequency range (Figures 8c and 8d), we see dominant fundamental and first-order Rayleigh wave energy at acausal times, which means energy is generally coming from the south. This is in agreement with the finding that energy from the coastline dominates the ambient noise field at low frequencies (Chang et al., 2013). Looking at the higher frequency range (Figures 8a and 8b), we see body-wave energy that is generally found at causal times, which is opposite what we see at the lower frequency range. Thus, body waves appear to be generated from inland rather than from the ocean. More specifically, body waves seem to be generated more from the north-northwest direction than the north direction, as the body wave is much weaker in Figure 8b than in Figure 8a.

Localization

Having determined that the body-wave energy is generated from the north-northwest direction, we now want to determine where they are most clear in the array. To find this, we create virtual super-source gathers using square patches of receivers centered along a regular grid with 0.75-km spacing (indicated by circles in Figure 10). We want to find the minimum patch size, and hence minimum number of virtual-source gathers, needed to resolve body waves for each patch location. Patch sizes begin at 2×2 km and progressively increase by 1 km on each side until a body wave can

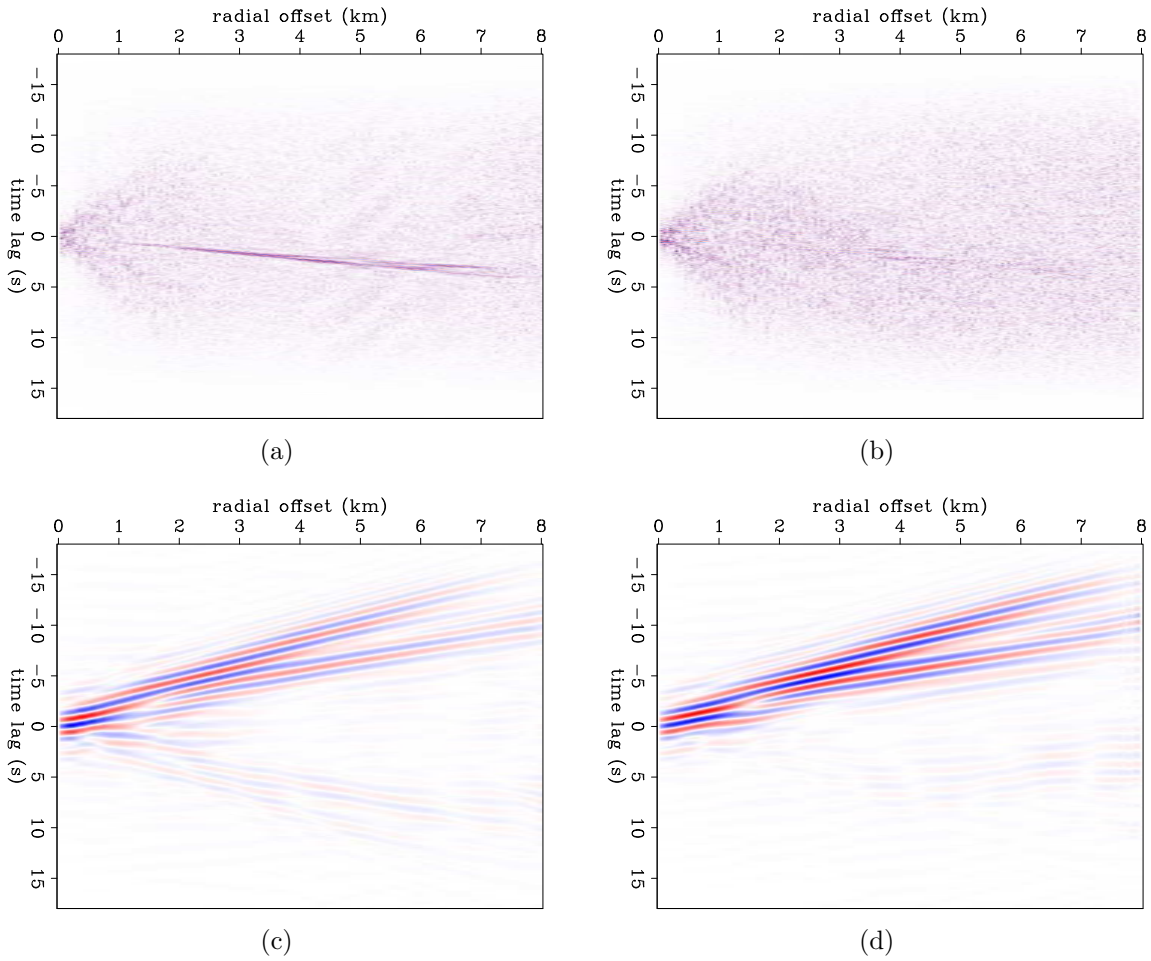

Figure 8: Virtual super-source gathers over two source-receiver azimuth ranges and two frequency ranges. Left column: azimuths between −55 and −65 degrees (receivers southeast of the virtual source). Right column: azimuths between −95 and −85 degrees (receivers south of the virtual source). Top row: 4.0-9.0 Hz. Bottom row: 0.5-2.0 Hz. [**CR**]

be resolved. The smaller the patch size that is needed to identify a body wave, the stronger the body-wave energy is in that region.

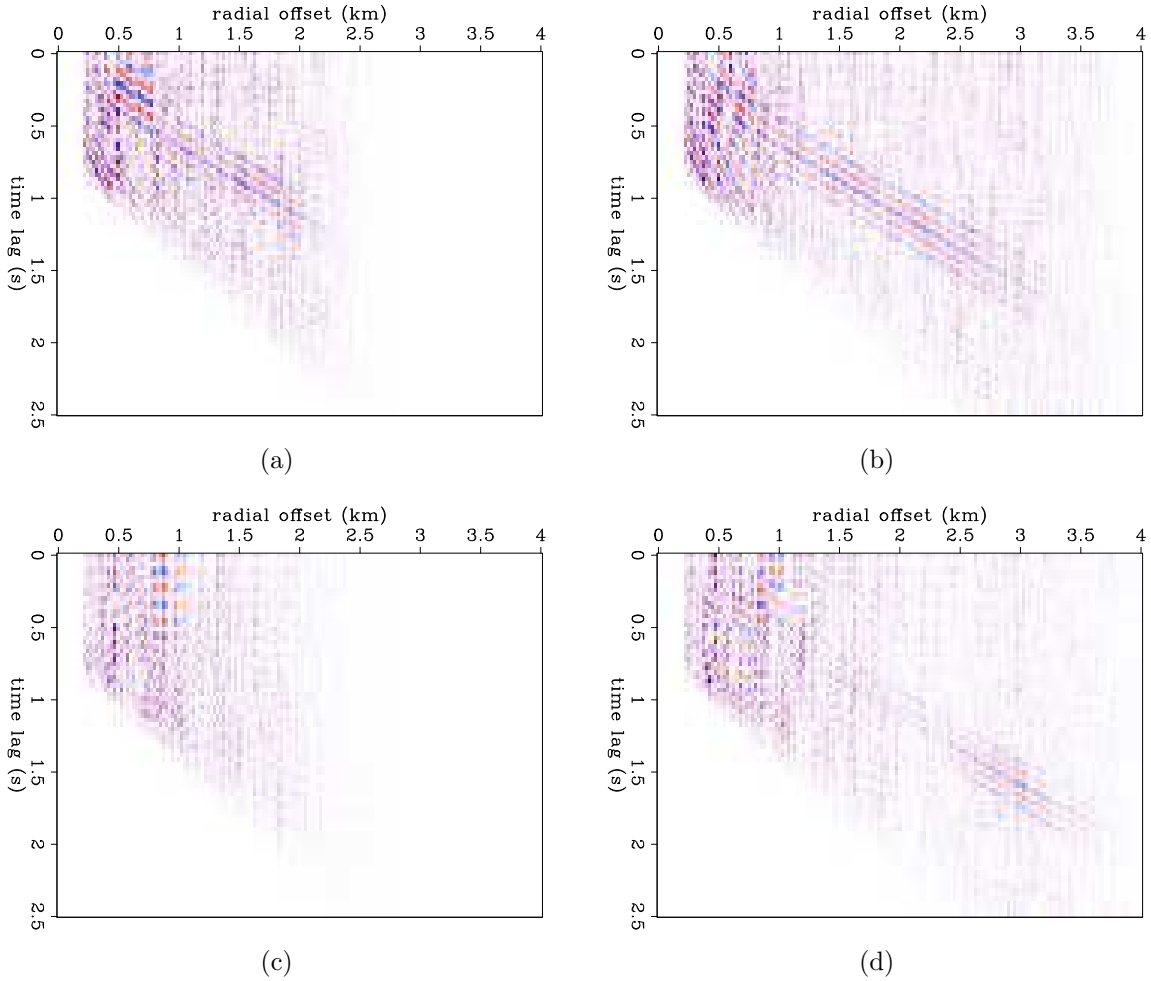

Figure 9: Examples of virtual super-source gathers over different patches of receivers. Top row: patches centered at (1295 km, 1230 km). Bottom row: patches centered at (1295.75 km, 1230.75 km). Left column: 2×2 km patches. Right column: 3×3 km patches. [**CR**]

The effect of patch size on body-wave resolution is shown in Figure 9. The top row corresponds to grid point (1295 km, 1230 km), while the bottom row corresponds to grid point (1295.75 km, 1230.75 km). The left column corresponds to 2×2 km patches, while the right column corresponds to 3×3 km patches. The patch size directly determines the maximum offset we see in the data; for instance, small patches have short maximum offsets. We see that at one location, the body wave is apparent with the smaller patch size, while at the other location, it is apparent only when increasing the patch size.

The minimum patch size needed to resolve body waves at each grid point is shown in Figure 10. Green dots represent regions that need a 2×2 km patch to resolve body

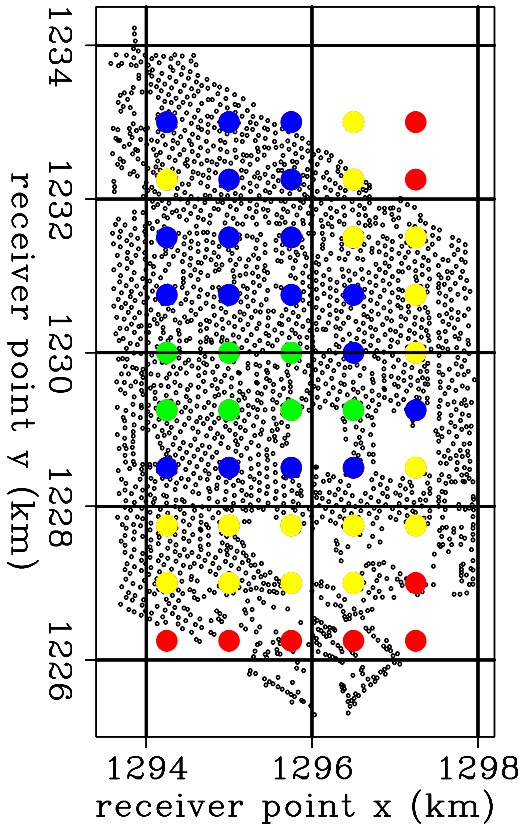

Figure 10: Map of centers of square patches used to determine where the body wave is the strongest. Colors correspond to the minimum patch size needed to see body waves. Green: 2×2 km, blue: 3×3 km, yellow: 4×4 km, red: 5×5 km. [**ER**]

waves (hence where body waves are most apparent), blue dots a 3×3 km patch, yellow dots a 4×4 km patch, and red dots a 5×5 km patch. This map suggests that body waves are best-resolved in the center of the array and then become progressively more difficult to distinguish toward the edges of the array. While low-quality patches along edges can be attributed to the limited number of receivers, the reason for low-quality patches around Interstate 405 is less clear. One possible explanation is that a dominant source of energy (the highway) runs through these patches. Therefore, strong noise sources are not found in the stationary-phase locations for many of the virtual source-receiver pairs. This can create strong spurious energy that masks the body-wave energy. Alternatively, patches showing clear body waves do not contain a single dominant energy source. Instead, they contain mostly traffic noise from local roads, which corresponds to noise sources that are better equipartitioned. This limits the effect of spurious energy that would potentially mask the body-wave energy.

The actual source of this body-wave energy is difficult to infer, despite determining that it comes dominantly from the north-northwest direction and that it is best-resolved in the center of the array. Given that traffic noise is strong at these frequencies, it is possible that this energy is generated at highways and local roads. Another possible source is the city of Los Angeles. It is located north-northwest of the array and is likely a very strong source of anthropogenic energy. Regardless of the true source, it is encouraging that we can retrieve body waves that could eventually be used for refraction tomography.

CONCLUSIONS AND FUTURE WORK

We showed that we can recover both surface waves and body waves for frequencies between 3–9 Hz. From a line of receivers running north-south, we confirm that energy in this frequency range is primarily generated by busy roads and highways. Group-velocity dispersion images and plots of arrival times as a function of azimuth suggest that recovered Rayleigh waves at these frequencies can be reliable enough for use in a transmission tomography workflow, particularly when either the virtual source or the receiver is near the highway. By summing over all virtual source gathers, we were able to recover body waves that appear to be diving and refraction events. When sorting correlation results by virtual source-receiver azimuth, we found that the body-wave energy is generated north-northwest of the array. After constructing virtual super-source gathers from patches of receivers across the array, we found that body waves are most apparent in the center of the array.

Our future work will focus on using high-frequency Rayleigh waves generated by Interstate 405 to perform a 2D tomography. Velocities at such shallow depths are valuable to fields such as earthquake hazard analysis. We will need to determine a method for selecting the most reliable EGFs for this purpose, but it appears that we will be able to use estimated arrival times from multiple azimuths and from virtual sources and receivers near the highway. Thus, the goal will be to produce group velocity maps for both sides of the highway.

ACKNOWLEDGMENTS

We thank Signal Hill Petroleum, Inc. for access to this dataset and permission to publish. Thanks to Dan Hollis for his cooperation and enthusiasm throughout this research. Thanks to Stew Levin, Bob Clapp, and Nori Nakata for their help handling the data and for numerous conversations.

REFERENCES

Bensen, G., M. Ritzwoller, M. Barmin, A. Levshin, F. Lin, M. Moschetti, N. Shapiro, and Y. Yang, 2007, Processing seismic ambient noise data to obtain reliable broadband surface wave dispersion measurements: Geophysical Journal International, **169**, 1239–1260.

Bensen, G., M. Ritzwoller, and N. Shapiro, 2008, Broadband ambient noise surface wave tomography across the United States: Journal of Geophysical Research: Solid Earth (1978–2012), **113**.

Chang, J. P., S. de Ridder, and B. Biondi, 2013, Power spectral densities and ambient noise cross-correlations at Long Beach: SEG Technical Program Expanded Abstracts.

Lin, F.-C., D. Li, R. Clayton, and D. Hollis, 2012, Interferometry with a dense 3D dataset: SEG Technical Program Expanded Abstracts, **1**, 1–6.

Lin, F.-C., D. Li, R. W. Clayton, and D. Hollis, 2013, High-resolution 3D shallow crustal structure in Long Beach, California: Application of ambient noise tomography on a dense seismic array: Geophysics, **78**, Q45–Q56.

Poli, P., M. Campillo, H. Pedersen, et al., 2012, Body-wave imaging of Earth's mantle discontinuities from ambient seismic noise: Science, **338**, 1063–1065.

Roux, P., K. G. Sabra, P. Gerstoft, W. Kuperman, and M. C. Fehler, 2005, P-waves from cross-correlation of seismic noise: Geophysical Research Letters, **32**.

Wapenaar, K., D. Draganov, R. Snieder, X. Campman, and A. Verdel, 2010, Tutorial on seismic interferometry: Part 1–basic principles and applications: Geophysics, **75**, 75A195–75A209.

Wapenaar, K. and J. Fokkema, 2006, Green's function representations for seismic interferometry: Geophysics, **71**, SI33–SI46.

Yang, Y., M. H. Ritzwoller, F.-C. Lin, M. Moschetti, and N. M. Shapiro, 2008, Structure of the crust and uppermost mantle beneath the western United States

revealed by ambient noise and earthquake tomography: Journal of Geophysical Research: Solid Earth (1978–2012), **113**.

Zhan, Z., S. Ni, D. V. Helmberger, and R. W. Clayton, 2010, Retrieval of Moho-reflected shear wave arrivals from ambient seismic noise: Geophysical Journal International, **182**, 408–420.